

Image Anomaly Detection and Localization with Position and Neighborhood Information

Jaehyeok Bae
Seoul National University

1 Gwanak-ro, Gwanak-gu, Seoul 08826
wogur110@snu.ac.kr

Jae-Han Lee
Gauss Labs Inc.

230 Homer Ave, Palo Alto, CA 94301
jaehan.lee@gausslabs.ai

Seyun Kim
Gauss Labs Inc.

230 Homer Ave, Palo Alto, CA 94301
seyun.kim@gausslabs.ai

Abstract

Anomaly detection and localization are essential in many areas, where collecting enough anomalous samples for training is almost impossible. To overcome this difficulty, many existing methods use a pre-trained network to encode input images and non-parametric modeling to estimate the encoded feature distribution. In the modeling process, however, they overlook that position and neighborhood information affect the distribution of normal features. To use the information, in this paper, the normal distribution is estimated with conditional probability given neighborhood features, which is modeled with a multi-layer perceptron network. At the same time, positional information can be used by building a histogram of representative features at each position. While existing methods simply resize the anomaly map into the resolution of an input image, the proposed method uses an additional refine network that is trained from synthetic anomaly images to perform better interpolation considering the shape and edge of the input image. For the popular industrial dataset, MVTec AD benchmark, the experimental results show **99.52%** and **98.91%** AUROC scores in anomaly detection and localization, which is state-of-the-art performance.

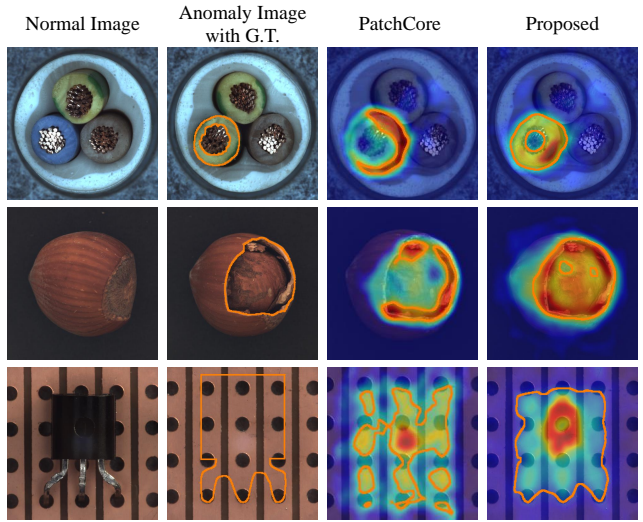


Figure 1. Examples from MVTec AD [2]. The normal images (left) and the anomalous images (second column) overlaid by ground truth mask are followed by the anomaly maps from PatchCore [18] (third column) and our proposed approach (right). The contours overlaid on anomaly maps are from thresholds optimizing F1 scores of anomaly localization.

shown in Figure 1.

1. Introduction

In some areas such as industrial manufacturing [2], collecting abnormal samples is very difficult, which makes building a supervised model for the task almost impossible. Anomaly detection methods make it possible to use only normal samples, where feature encoding and statistical modeling for the normal features are commonly performed. Anomaly localization is to quantify anomaly of every pixel in an input image, which makes users can find where the anomaly is located and the models explainable. Some example images and results of an existing method and our proposed approach from the MVTec AD benchmark dataset are

Because there are only normal samples to train, common classification methods cannot be used. One approach is distribution-based methods, in which generative models such as auto-encoder [4, 16, 22] and GAN (generative adversarial networks) [1, 17, 21] are trained to learn nominal statistical distribution. At inference time, test images are reconstructed from the trained normal distribution to follow the similar ones in normal images. Recently, flow-based methods [7, 19, 28] have been proposed and show good performance especially in texture type images, which train normalizing flow models to learn the distribution of encoded normal features. Among them, CFLOW-AD [7] adopts positional encoding to model conditional distribution according to the position of feature, but the effect in object type

images is not explicitly proved.

Other methods [14,27] generate synthetic abnormal samples from normal dataset and train encoder to transform input samples into features. Among them, CutPaste [14] used masks of rectangular and scar shapes to learn representation in a self-supervised manner. These approaches, however, show relatively low performance compared to recent methods since mimicking abnormal patterns as real images is difficult. To overcome the difficulty of learning representation, many recently proposed methods [5,18] adopt a pre-trained network such as ImageNet [20] trained Resnet [9], which intensively learned low-level image features from a super large-sized dataset.

With normal features transformed by a pre-trained network, the distribution is modeled by various methods. PatchCore [18] samples representative features, coreset, from extracted normal features, and stores them in a memory bank, which is non-parametric modeling of nominal features. For the features from test images, anomaly scores are calculated by measuring the distance to the nearest element of the stored coreset features, or the estimated distribution of normal features from train images. In this process, support region of feature, or patch size, is an important hyper-parameter. Too large patch ignores small anomaly regions like scratch, and too small patch cannot catch large structure aberration or semantic change. Also, putting all normal features in a memory bank, position and neighborhood information disappears and cannot be used to model their complex relationship. For example in the first row in Figure 1, top-view cables are normal when the order of color is correct like the image of the first column. However, if the order of color is incorrect so that the color of the lower-left cable is green like the image of the second column, this cable is an abnormal area although local features are normal. Existing representation-based approaches such as PatchCore cannot capture these abnormal areas, which leads to performance degradation of anomaly detection and localization.

In this paper, to address the problem, position and neighborhood information are utilized in simple but effective ways. To be more specific, the representative set of normal features, called a coreset, is generated by sampling local features of training images. At each position of the encoded feature dimension, a probability distribution of the coreset features is modeled by building a histogram from all the features of training images. At the same time, a probability distribution of normal features conditioned by neighboring features is modeled by MLP (multi-layer perception) network, which is fed by concatenated neighboring features and estimates the likelihood of each coreset feature. Through this process, the MLP network observes a large support region, but the features are still local, which makes the aforementioned patch size problem solved. The two dis-

tributions are combined to estimate the likelihood and score of an input image and its pixels at test time. Ablation study shows that two kinds of position and neighborhood information are both useful for performance improvement.

In addition to position and neighborhood information, representation-based approaches have a limitation in depicting detailed anomaly maps since local features from a pre-trained model are patch-level, and contain a small area of pixels. Patch-level anomaly map is reshaped to calculate the pixel-level anomaly map, which misses pixel-wise details. To alleviate this problem, we trained an additional refine network with synthetic abnormal images from the normal training dataset. Random shapes and sizes of patches in train images are replaced by patches from other images, which represent abnormal areas. With synthetic images and corresponding anomaly maps generated using position and neighborhood information mentioned above, refine network learns how to revise anomaly map into look like ground truth mask.

To summarize, our main contributions are (i) showing the effectiveness of using conditional normal feature distribution from position and neighborhood information in anomaly detection and localization, (ii) conducting ablation studies on the effect of position and neighborhood information, and (iii) verifying training refine network from synthetic dataset enhances the performance.

2. Related work

PatchCore [18] has a typical structure of representation-based approaches and shows outstanding performance in anomaly detection and localization. PatchCore aggregates whole local patch features from normal train data and subsamples them into a representative subset with greedy coreset subsampling. At test time, the pixel-wise anomaly score for each patch feature from a test image is calculated by nearest neighbor search from coreset. The maximum of test patch features calculates image anomaly scores of test images. The proposed method uses the typical structure of making patch features with a pre-trained network and non-parametric modeling of normal feature distribution. The common part of PatchCore and our method is explained in this section.

All images x_i in training dataset \mathcal{X}_N are normal ($y(x_i) = 0$), and images x_t in test dataset \mathcal{X}_T can be normal ($y(x_t) = 0$) or anomalous ($y(x_t) = 1$). At train time, with pre-trained network ϕ , all train images $\forall x_i \in \mathcal{X}_N$ are converted to hierarchical features $\phi_{i,j} = \phi_j(x_i)$, where j is hierarchy level of pretrained network ϕ . For example in ResNet-50 [9], $j \in \{1, 2, 3, 4\}$ indicates the final output of each resolution blocks. We note feature map $\phi_{i,j} \in \mathbb{R}^{c^j \times h^j \times w^j}$ as a three-dimensional tensor, where c^j , h^j , and w^j are the number of channels, height, and width, respectively. To avoid using too high or low-level features,

intermediate features, $\phi_{i,2}$ and $\phi_{i,3}$ are concatenated and used. Because their spatial size (h, w) is different, the smaller one is resized to be the same size of the larger one: (h^*, w^*) , $h^* = \max(h_2, h_3)$, $w^* = \max(w_2, w_3)$, and they are concatenated into $\phi_i^* \in \mathbb{R}^{c^* \times h^* \times w^*}$, which $c^* = c_2 + c_3$. In addition, to increase the receptive field of feature maps, pixel-level feature $\Phi_i(h, w)$ is extended to incorporate the neighborhood features within a specific patch size of p . The adaptive average pooling is performed to output one single feature of dimension d at (h, w) . Through this process, train images $x_i \in \mathcal{X}_N$ are converted into a set of local patch-level features $\Phi_i \in \mathbb{R}^{d \times h^* \times w^*}$.

All patch-level features Φ_i from all train images are gathered into a memory bank \mathcal{M} . The features in the memory bank are subsampled via iterative greedy approximation algorithm [24], which leads to coreset \mathcal{C} . This process reduces the number of features processed in the inference time and makes the inference carried out in practical time. Also, the subsampling removes outliers and makes the model more generalizable.

At inference time, each test image $x_t \in \mathcal{X}_T$ is transformed into patch-level features Φ_t with the same process as the normal train features Φ_i . For each feature $\Phi_t(h, w) | \exists h \in [0, h^*), \exists w \in [0, w^*)$, pixel-level anomaly score is calculated from nearest neighborhood distance between $\Phi_t(h, w)$ and coreset \mathcal{C} , which is noted as $d(h, w)$. Based on the fact that the normal distribution of patch-level features is represented as coreset \mathcal{C} , $d(h, w)$ represents how far $\Phi_t(h, w)$ is from the normal distribution. In addition, the image-level anomaly score is calculated as the maximum score among all pixel-level anomaly scores $d(h, w)$ in the image.

Note that position and neighborhood information is not used after local features are collected into the memory bank. However, as can be seen in Figure 1, a feature can be normal or abnormal according to its position or what features are surrounding it. This paper proposes an algorithm considering the position and neighborhood information. In experiments, we demonstrate that this approach correctly estimates the abnormality of test features miscalculated only with local information.

3. Method

3.1. Overview

Let \mathbf{x} be the spatial coordinate (h, w) . Most existing representation-based methods calculate anomaly score of pixel-level feature $\Phi_i(\mathbf{x})$ with trained distribution of normal features and $\Phi_i(\mathbf{x})$ itself. Letting a probability of feature $\Phi_i(\mathbf{x})$ to be normal as $p(\Phi_i(\mathbf{x}))$, anomaly score of respective position $S(\mathbf{x})$ can be represented as negative log likelihood of $p(\Phi_i(\mathbf{x}))$ as

$$S(\mathbf{x}) = -\log p(\Phi_i(\mathbf{x})). \quad (1)$$

In contrast, anomaly score of $\Phi_i(\mathbf{x})$ is dependent on neighborhood features and position of the feature in the whole image x_i . For example in Figure 1, transistors in the normal dataset are located in the center of images (the left image of the third row) and electric wires are located in their sheath (the left image of the first row). Therefore, when we note position and neighborhood information as Ω , anomaly score of $\Phi_i(\mathbf{x})$, $S(\mathbf{x})$, can be represented as negative log-likelihood of conditional probability of $\Phi_i(\mathbf{x})$ given Ω :

$$S(\mathbf{x}) = -\log p(\Phi_i(\mathbf{x}) | \Omega). \quad (2)$$

In this paper, $p(\Phi_i(\mathbf{x}) | \Omega)$ is approximated with most probable coreset feature given circumstance Ω as follows:

$$\begin{aligned} p(\Phi_i(\mathbf{x}) | \Omega) &= \sum_{c \in \mathcal{C}_{\text{dist}}} p(\Phi_i(\mathbf{x}) | c, \Omega) p(c | \Omega) \\ &\approx \max_{c \in \mathcal{C}_{\text{dist}}} p(\Phi_i(\mathbf{x}) | c, \Omega) p(c | \Omega), \end{aligned} \quad (3)$$

where $\mathcal{C}_{\text{dist}}$ is the distribution coreset of normal features, which will explain below. For each coreset element c , $p(\Phi_i(\mathbf{x}) | c, \Omega)$ indicates the probability of $\Phi_i(\mathbf{x})$ to be normal given coreset feature c with position and neighborhood information Ω , and $p(c | \Omega)$ indicates the probability of c to be normal feature given Ω . We note $p(c | \Omega)$ as normal feature distribution. At train time, normal feature distribution in conditions of neighborhood and position information is trained with MLP and histogram respectively as shown in Figure 2, an overview of our proposed approach. At inference time, $p(\Phi_i(\mathbf{x}) | \Omega)$ is calculated with the corresponding Ω and the trained normal feature distribution.

Since the resolution of the feature score map, (h^*, w^*) , is different from the original input resolution (H, W) , it is resized by bi-linear interpolation, and is smoothed by Gaussian kernel of $\sigma = 8$ to generate natural anomaly map. The parameter σ is not intensively optimized. At the last, pixelwise refinement step is followed to enhance the resized score map more conformable to the edge, texture, and shape of the input image.

3.2. Modeling Normal Feature Distribution

As described in Section 2, all train images $x_i \in \mathcal{X}_N$ are encoded to feature map Φ_i and total feature vectors $\forall \Phi_i(\mathbf{x})$ are stored to memory bank \mathcal{M} . For outlier removal and efficient computation, feature vectors in the memory bank are subsampled to embedding coreset \mathcal{C}_{emb} using greedy coreset subsampling method [23]. Using this embedding coreset \mathcal{C}_{emb} , non-parametric distribution of normal features is modeled. This coreset \mathcal{C}_{emb} is subsampled again to make distribution coreset $\mathcal{C}_{\text{dist}}$, with which we can estimate $p(\mathcal{C}_{\text{dist}} | \Omega)$, the probability of an element of distribution coreset conditioned by neighborhood information. The probability $p(\mathcal{C}_{\text{dist}} | \Omega)$ is modeled by multi-layer perceptron

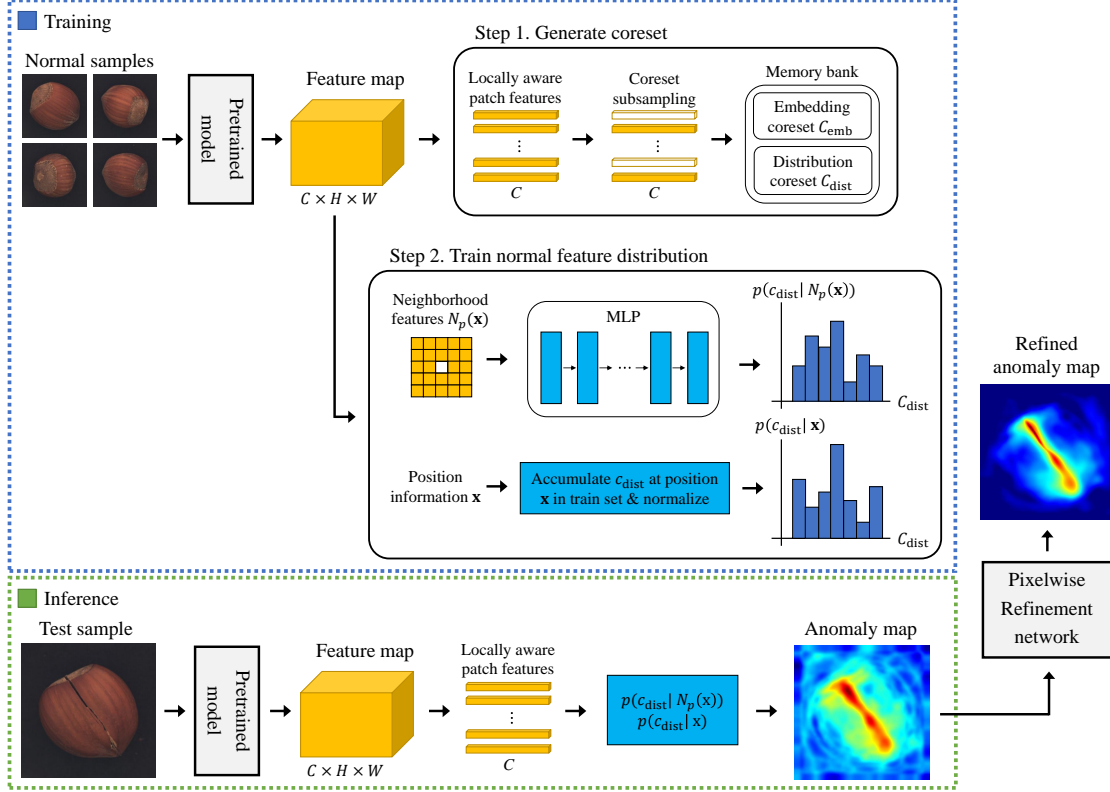


Figure 2. Overview of our proposed approach using position and neighborhood information. At train time, normal samples are converted to feature map Φ_i using ImageNet pre-trained model ϕ . Aggregated patch-level features are subsampled to generate embedding coreset C_{emb} and distribution coreset C_{dist} using greedy subsampling method. After storing the coresets, normal feature distribution given neighborhood and position information is trained with MLP and histogram respectively. At inference time, anomaly score for local test feature is evaluated using the trained normal feature models. At last, the refinement step is performed to improve the anomaly map considering the input image.

(MLP) network, and the size of the distribution coreset cannot be large since training efficiency will decrease.

To model $p(c_{\text{dist}}|\Omega)$, neighboring features $N_p(\mathbf{x})$ of input feature $\Phi_i(\mathbf{x})$ are fed to a simple MLP network. The neighboring features $N_p(\mathbf{x})$ is a set of features that are within $p \times p$ patch except \mathbf{x} itself and is defined as follows:

$$N_p(\mathbf{x}) = \{\Phi_i(m, n) \mid |m - h| \leq p/2, |n - w| \leq p/2, (m, n) \neq (h, w)\}, \quad (4)$$

where $\Phi_i(m, n)$ is feature vector at position (m, n) in the feature map Φ_i . To model $p(c_{\text{dist}}|N_p(\mathbf{x}))$, the simple MLP is fed by an input that is a 1-dimensional vector of concatenated all features in $N_p(\mathbf{x})$. It consists of N_{MLP} sequential layers with c_{MLP} channels, and includes batch normalization and ReLU activation functions in between layers. It models a probability mass function of distribution coreset C_{dist} to be normal given condition of $N_p(\mathbf{x})$. In other words, the output of MLP has $|C_{\text{dist}}|$ nodes and value of each node represents the probability of the corresponding distribution coreset feature. Generally, trained deep neural network models tend to be overconfident, which means their softmax values are biased towards 0 and 1. Therefore, we

applied temperature scaling [8] with temperature $T = 2$ so that the likelihood values be realistic.

Position information (\mathbf{x}) is also important, which affects the probability of $\Phi_i(\mathbf{x})$ to be normal feature especially in some object type images. To train $p(c_{\text{dist}}|\mathbf{x})$, we accumulate the index of C_{dist} for each position (\mathbf{x}) in all train images $\forall x_i \in X_N$ as histogram. In the process, features in $p \times p$ neighborhood are counted for robust estimation. The conditional distribution given position and neighborhood information $p(c_{\text{dist}}|\Omega)$ is approximated as an average of the two probability $p(c_{\text{dist}}|\mathbf{x})$ and $p(c_{\text{dist}}|N_p(\mathbf{x}))$ as:

$$p(c_{\text{dist}}|\Omega) \approx \frac{p(c_{\text{dist}}|\mathbf{x}) + p(c_{\text{dist}}|N_p(\mathbf{x}))}{2}. \quad (5)$$

To calculate $p(\Phi_i(\mathbf{x})|c_{\text{dist}}, \Omega)$ in (3), we assume that $(\Phi_i(\mathbf{x})|c_{\text{dist}})$ is independent on Ω , since if c_{dist} is given, $\Phi_i(\mathbf{x})$ should be close to c_{dist} to be normal feature whatever Ω looks like. Also, $(\Phi_i(\mathbf{x})|c_{\text{dist}})$ is approximated with the distance between $\Phi_i(\mathbf{x})$ and c_{dist} , which can be interpreted as short distance between two vectors leads to proximity of them. With these assumptions, $p(\Phi_i(\mathbf{x})|c_{\text{dist}}, \Omega)$ is

expressed as follows:

$$p(\Phi_i(\mathbf{x})|c_{\text{dist}}, \Omega) \approx p(\Phi_i(\mathbf{x})|c_{\text{dist}}) \approx e^{-\lambda \|\Phi_i(\mathbf{x}) - c_{\text{dist}}\|_2}. \quad (6)$$

We set the probability $p(\Phi_i(\mathbf{x})|c_{\text{dist}})$ as an exponential function given the assumption that $(\Phi_i(\mathbf{x})|c_{\text{dist}})$ is only affected by distance between $\Phi_i(\mathbf{x})$ and c_{dist} . λ is a hyper-parameter of an exponential function, and we set $\lambda = 1$ without optimizing.

In the modeling of $p(c_{\text{dist}}|N_p(\mathbf{x}))$ in (3) with MLP network, the cardinality $|C_{\text{dist}}|$ should be small so that the model can be trained with a moderate number of normal training images. With the small size of the distribution coreset, however, accurate estimation of $p(\Phi_i(\mathbf{x})|c_{\text{dist}}, \Omega)$ is difficult, so the new large size of embedding coreset C_{emb} is introduced. We first calculated nearest element c_{emb} in C_{emb} from each distribution coreset index $\exists c_{\text{dist}} \in C_{\text{dist}}$ and approximates $p(\Phi_i(\mathbf{x})|c_{\text{dist}}, \Omega)$ in (6) as follows:

$$c_{\text{emb}}^* = \underset{c \in C_{\text{emb}}}{\operatorname{argmin}} \|c - c_{\text{dist}}\|_2, \quad (7)$$

$$p(\Phi_i(\mathbf{x})|c_{\text{dist}}, \Omega) \approx e^{-\lambda \|\Phi_i(\mathbf{x}) - c_{\text{emb}}^*\|_2}. \quad (8)$$

We replaced c_{dist} to c_{emb}^* in (8) given the assumption that c_{dist} and c_{emb}^* are similar enough. With (8), (3) changes as follows:

$$\begin{aligned} p(\Phi_i(\mathbf{x}) | \Omega) &= \max_{c \in C_{\text{dist}}} p(\Phi_i(\mathbf{x}) | c, \Omega) p(c | \Omega) \\ &\approx \max_{c \in C_{\text{dist}}} \left(e^{-\lambda \|\Phi_i(\mathbf{x}) - c_{\text{emb}}^*\|_2} p(c | \Omega) \right). \end{aligned} \quad (9)$$

Since (9) is computationally intractable, we quantized $p(c | \Omega)$ into a binary value assuming coreset features with certain probability are equally normal. To address this, we defined threshold function $T(x, \tau)$ with threshold hyperparameter τ as follows:

$$T(x, \tau) = \begin{cases} 1, & \text{if } x > \tau \\ 0, & \text{otherwise,} \end{cases} \quad (10)$$

and (9) is changed as follows:

$$\begin{aligned} p(\Phi_i(\mathbf{x}) | \Omega) \\ \approx \max_{c \in C_{\text{dist}}} \left(e^{-\lambda \|\Phi_i(\mathbf{x}) - c_{\text{emb}}^*\|_2} T(p(c | \Omega), \tau) \right). \end{aligned} \quad (11)$$

τ lower than $1/|C_{\text{dist}}|$ guarantees at least one of c in C_{dist} be a normal feature. In this paper, we set $\tau = 1/(2|C_{\text{dist}}|)$ without optimizing.

3.3. Pixelwise Refinement

As shown in Figure 2, the proposed algorithm estimates an anomaly map for an input image. We further improve the reliability of the anomaly map by using a refinement

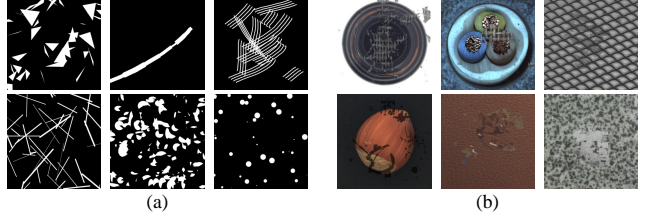


Figure 3. Examples of (a) defect patch patterns which are created in a hand drawing manner, and (b) artificially generated anomaly images in pixelwise refinement process.

network f , trained in a supervised manner using an artificially created defect dataset \mathcal{D} . Let θ be parameters of f . We aim at training optimal parameters

$$\theta^* = \arg \min_{\theta} \sum_{(I, \hat{A}, A) \in \mathcal{D}} \ell(f(I, \hat{A}; \theta), A). \quad (12)$$

\mathcal{D} is composed of (I, \hat{A}, A) pairs. I is an artificially generated anomaly image, A represents the ground-truth anomaly map of I , with 1 assigned to defect regions and 0 assigned to others. \hat{A} is an anomaly map estimated from the proposed algorithm. We normalize each map into $[0, 1]$ in the same way with [18]. ℓ is a loss function between the refine $\tilde{A} \triangleq f(I, \hat{A}; \theta)$ and the ground-truth A .

Each data in \mathcal{D} is generated by exploiting the training images of MVTec AD. Figure 3 shows generation process examples of data. First, we make the defect pattern in the form of a binary patch. To give the patch pattern variety, we created the patch shapes in a hand drawing manner, as shown in Figure 3(a). Next, we generate a more complicated defect label A by randomly resizing patterns and combining them. Finally, I is given by

$$I = (1 - A) \odot I_{\text{clean}} + A \odot I_{\text{defect}}, \quad (13)$$

where \odot is Hadamard product operation and I_{clean} is a normal image with no defects. I_{defect} is an image for the defect region of I , and we obtain it using randomly sampled images from the MVTec AD dataset. Figure 3(b) shows examples of I .

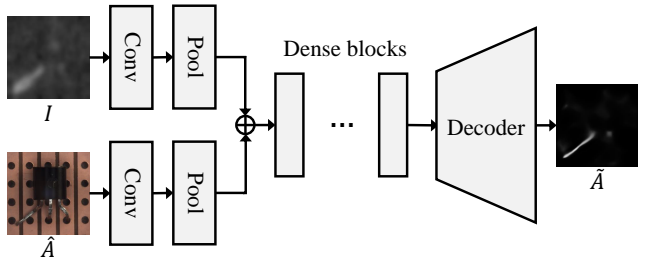


Figure 4. Schematic structure of the pixelwise refinement network.

Table 1. Anomaly Detection and localization AUROC score on MVTec AD. The first and the second numbers are detection and localization scores, respectively. We provided sub-total averages for object and texture type classes.

		CFLOW-AD [7]	PatchCore [18]	FastFlow [28] (WRN50)	FastFlow (CaiT)	Proposed (w/o refine)	Proposed
Object	Bottle	(100, 98.76)	(100, 98.6)	-	(100, 97.7)	(100, 98.94)	(100, 98.98)
	Cable	(97.59, 97.64)	(99.5, 98.4)	-	(100, 98.4)	(99.59, 99.13)	(99.78, 99.14)
	Capsule	(97.68, 98.98)	(98.1, 98.8)	-	(100, 99.1)	(99.40, 99.25)	(99.52, 99.30)
	Hazelnut	(99.98, 98.82)	(100, 98.7)	-	(100, 99.1)	(99.59, 99.49)	(100, 99.17)
	Metal nut	(99.26, 98.56)	(100, 98.4)	-	(100, 98.5)	(100, 99.39)	(100, 99.26)
	Pill	(96.82, 98.95)	(96.6, 97.1)	-	(99.4, 99.2)	(96.67, 99.06)	(97.19, 98.96)
	Screw	(91.89, 98.10)	(98.1, 99.4)	-	(97.8, 99.4)	(99.51, 99.59)	(98.87, 99.41)
	Toothbrush	(99.65, 98.56)	(100, 98.7)	-	(94.4, 98.9)	(100, 99.09)	(99.72, 99.08)
	Transistor	(95.21, 93.28)	(100, 96.3)	-	(99.8, 97.3)	(100, 97.97)	(100, 98.42)
		(97.56, 97.96)	(99.14, 98.27)	-	(99.04, 98.62)	(99.42, 99.10)	(99.45, 99.08)
Texture	Carpet	(98.73, 99.23)	(98.7, 99.0)	-	(100, 99.4)	(99.68, 99.25)	(100, 99.39)
	Grid	(99.60, 96.89)	(98.2, 98.7)	-	(99.7, 98.3)	(98.58, 98.80)	(98.58, 98.92)
	Leather	(100, 99.61)	(100, 99.3)	-	(100, 99.5)	(100, 99.18)	(100, 99.53)
	Tile	(99.88, 97.71)	(98.7, 95.6)	-	(100, 96.3)	(100, 97.86)	(99.96, 98.34)
	Wood	(99.12, 94.49)	(99.2, 95.0)	-	(100, 97.0)	(99.47, 96.13)	(99.39, 96.46)
	Zipper	(98.48, 98.41)	(98.8, 98.8)	-	(99.5, 98.7)	(99.82, 99.31)	(99.82, 99.30)
		(99.30, 97.72)	(98.93, 97.72)	-	(99.87, 98.2)	(99.59, 98.42)	(99.63, 98.66)
Average		(98.26, 97.87)	(99.06, 98.05)	(99.3, 98.1)	(99.37, 98.45)	(99.49, 98.83)	(99.52, 98.91)

We adopt the encoder-decoder architecture for refinement network. We develop the network structure similar to the Lee and Kim’s network [13] using DenseNet161 [10] backbone, but we make two modifications. First, refinement network takes as 4 channel inputs of an RGB image I and an anomaly map \hat{A} . Second, following the early fusion method [11], we fused the features of I and \hat{A} after the first convolution layer. Figure 4 shows the schematic structure of the pixelwise refinement network.

To train f , we use a loss function consisting of two terms: $\ell = \ell_{\text{reg}} + \ell_{\text{grad}}$. The regression loss ℓ_{reg} is given by L2-norm between \hat{A} and A .

$$\ell_{\text{reg}} = \|\hat{A} - A\|_2 / (HW), \quad (14)$$

where H and W are the width and height of A . Next, the gradient loss ℓ_{grad} is

$$\ell_{\text{grad}} = (|\nabla_h \hat{A} - \nabla_h A|_2 + |\nabla_w \hat{A} - \nabla_w A|_2) / (HW), \quad (15)$$

where ∇_h and ∇_w are partial derivative operations in the vertical and horizontal directions, respectively. ℓ_{grad} improves the refinement results by making the network’s training more concentrated near the edges of the defect region.

4. Experimental Setup

4.1. Experimental Details

Datasets Our experiments are performed on popular industrial datasets to evaluate the effect of our approaches: MVTec AD [2] and BTAD [15] dataset. MVTec AD includes 15 sub-categories and total 5,354 images, where 3,629 images are train images which are all normal, and

1,725 test images consist of both normal and anomalous images with ground truth mask. Anomaly images are categorized with various kinds of defects. BTAD is also industrial anomaly detection dataset with 3 sub-categories and total 2,830 real-world images, among which 1,800 images are for training.

As in [3, 5, 18, 27], images of all datasets are resized, and center cropped to eliminate negligible image boundary pixels. In MVTec AD, images are resized to 512×512 and center cropped to 480×480 . In BTAD, images are resized to 256×256 and center cropped to 224×224 since images in BTAD don’t contain a minute detail compared to MVTec AD. We didn’t use any data augmentation since each category has different permissible augmentation based on the characteristics of the images.

Evaluation Metrics As in previous works such as [7, 18, 28], we evaluated the performance of the model via the area under the receiver operator curve (AUROC). To evaluate image anomaly detection performance, AUROC score is measured from a single anomaly score for each test image and the respective ground truth. In addition, to evaluate pixel-wise anomaly localization performance, AUROC score is measured using pixel-wise anomaly map and corresponding ground truth map.

Because typical anomalous regions are much smaller than normal regions, localization AUROC scores tend to be high, but small variation in the error affects the pixel segmentation results. Also, the detection AUROC scores are high, but it is still not satisfactory because very high sensitivity is required in industrial manufacturing. Increasing sensitivity arises in an increased false alarm rate, which again increases the cost of manual inspection.

Parameter Setup In the single model training, we used pre-trained Wideresnet-101 [29] as a feature extractor. ResNext-101 [26] and DenseNet-201 [10] are additionally exploited in the ensemble model training. In generation of local patch-level features, pixel-level feature is extended to aggregate with neighborhood features within a patch size of 5, and average pooling is performed to output one single feature vector of dimension $d = 1024$, which is same as [18]. Subsampling percentage to generate embedding coreset is 1%, and the size of distribution coreset $|C_{\text{dist}}|$ is set to 2048.

In the process of training $p(c_{\text{dist}}|\mathbf{x})$ and $p(c_{\text{dist}}|N_p(\mathbf{x}))$, we set patch size of neighborhood $p = 9$. The MLP network for the normal feature distribution consists of 10 fully-connected layers and each layer includes 2048 neurons. We train the MLP network using the Adam optimizer [12] for 15 epochs with a 10^{-3} learning rate and batch size 2048. Also, we adopt StepLR scheduler with $\gamma = 0.1$ and 5 step size. We train the refinement network using the Adam optimizer for 3 epochs with a 10^{-4} learning rate and batch size 8. Also, we perform data augmentation, including random horizontal flip, rotation, and color change in an online manner. In inference, we fuse the refined \hat{A} at a 10% ratio with \hat{A} to obtain the final anomaly map.

4.2. Quantitative Results on MVTec AD

The overall results for anomaly detection and localization performance on MVTec AD are shown in table 1. To verify the effect of refinement network, our model without refine network is reported as well as with refinement network. We compared the performance with the previous work, CFLOW-AD [7], PatchCore [18], and FastFlow [28], in terms of image-level AUROC and pixel-level AUROC. For a fair comparison, a single model for each algorithm is reported. As for CFLOW-AD, we brought the result from the original paper, which shows the highest performance among single models. In PatchCore, we took the results from the original paper. FastFlow uses both pre-trained CNN such as Wideresnet-50 and pre-trained transformer ViT [6] as a feature extractor. For unbiased observation, we reported both results of FastFlow using Wideresnet-50 and CaiT [25], which is a typical model for ViT. In table 1, we classified 15 categories on MVTec AD into Object and Texture, where repetitive patterns and texture exist and no background exists. Images in the object category have anomaly patches mainly inside the object, while the texture category can have anomaly patches anywhere. Our proposed approach with refinement model outperforms the state-of-the-art algorithm by 0.46% AUROC in localization and 0.17% AUROC in detection. Even without refinement network, in addition, our approach outperforms the existing works by 0.38% AUROC in localization and 0.12% AU-

Table 2. The Ablation Results on MVTec AD.

	Neighbor	Position	Detection	Localization
PatchCore	-	-	99.06	98.05
Proposed (w/o refine)	o	x	99.37	98.66
	x	o	99.48	98.76
	o	o	99.49	98.83
Proposed	o	o	99.52	98.91

ROC in detection.

As one can easily think, our motivation for using position and neighborhood information may be more beneficial in object type images, and the result supports the guess. The performance gain to the existing methods in object classes is larger than in texture classes, and there are considerable improvements for localization of transistor, metal nut, and bottle classes. As shown in the table, refinement network is more effective in the texture category, since performance is improved by 0.24% AUROC in localization and 0.04% AUROC in detection. This verifies that refining anomaly map through edge in images is critical for precise anomaly prediction in the texture category. Additionally, FastFlow with CaiT shows high performance in the light of a powerful transformer while noticeable performance drops in a few classes decrease the average score.

To verify the effect of using neighborhood and position information, the results of the ablation study are shown in Table 2. Note that any configuration of ablation study with our proposed model outperforms PatchCore with a single model in both anomaly detection and localization since PatchCore deals with normal features unconditionally.

In addition, the effect of the ensemble method and the proposed refinement is examined. Instead of Wideresnet-101 as a feature extractor, we trained the model with different feature extractors, ResNext-101 [26] and DenseNet-201 [10], respectively. Evaluated anomaly maps from 3 different feature extractors are averaged to generate an ensembled anomaly map, which is the same method as that of PatchCore. As shown in Table 3, the ensemble method of our proposed model with refine model performs 99.55% anomaly detection AUROC, which is closest to cutting-edge performance, and 99.05% anomaly localization AUROC, which is the state-of-the-art performance.

Table 3. The Ensemble Results on MVTec AD.

	Detection	Localization
CFLOW-AD	94.60	98.62
PatchCore	99.6	98.2
FastFlow	99.37	98.45
Proposed	99.55	99.05

4.3. Anomaly Localization on BTAD

The anomaly localization performances of our proposed model on BTAD are presented in Table 4. On BTAD, we

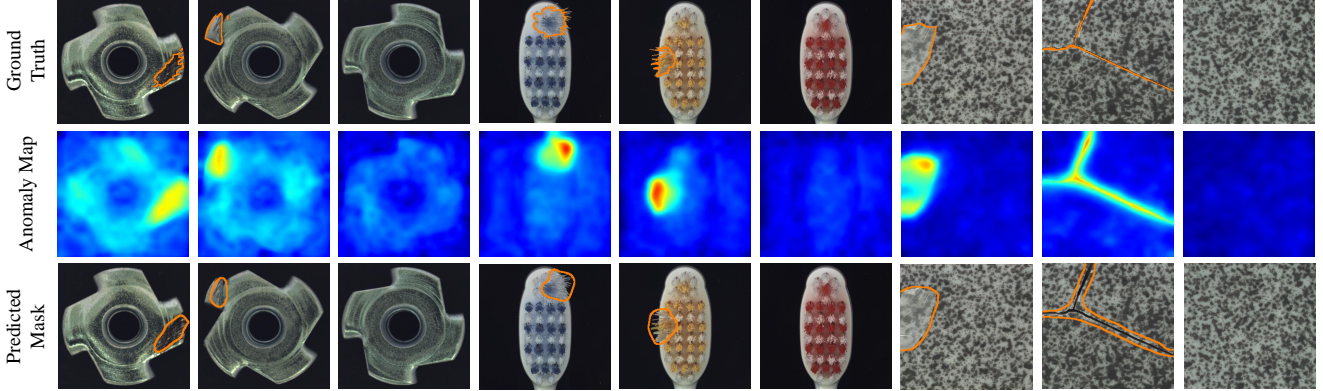


Figure 5. Examples of the test images, the anomaly maps, and the predicted masks on the MVTec AD. The ground truth anomaly masks are overlaid.

compared anomaly localization results with VT-ADL [15] and FastFlow [28]. For a fair comparison, we used our proposed single model without refinement. As shown in table 4, the proposed model outperforms other state-of-the-art algorithms by 0.8% AUROC in anomaly localization on BTAD.

Table 4. Anomaly localization results on BTAD.

	VT-ADL [15]	FastFlow [28]	Proposed (w/o refine)	Proposed
1	99	95	97.0	97.4
2	94	96	96.5	96.6
3	77	99	98.9	99.1
Average	90.0	96.7	97.5	97.7

4.4. Qualitative Results

We compare the anomaly map and predicted mask of our proposed model on various images of MVTec AD. Some examples from the MVTec AD and the respective anomaly maps are shown in Figure 5. The top row shows test images with ground truth masks, and the middle row represents corresponding anomaly maps estimated by the proposed model. We generated the contours of the predicted mask from thresholds optimizing F1 scores on anomaly map, and overlaid the contours on the corresponding test images, which are in the bottom row. We can observe that predicted masks on test images generally follow the ground truth, which leads to performance enhancement.

Figure 6 shows the histogram of pixel-wise anomaly scores for the metal_nut class from MVTec AD from PatchCore and our proposed model. The green and the red parts represent anomaly scores of normal and anomalous features respectively, and the blue vertical line shows the threshold optimizing F1 score. In 6, the red pixels on the left of the threshold are misclassified anomaly pixels, or false negative pixels. Likewise, the green pixels on the right of the threshold are false positive pixels. The false positive rate

and false negative rate of PatchCore, 3.4% and 10.7%, are decreased to 2.0% and 9.5% in the proposed method, which corresponds to the higher AUROC score of the proposed method.

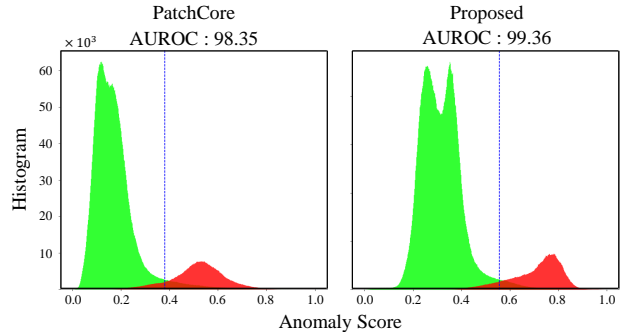


Figure 6. Histogram of anomaly scores of normal (green) and anomaly (red) pixels for the metal_nut class in MVTec AD evaluated by PatchCore (left) and our proposed model (right). The blue vertical line is the threshold optimizing F1 score.

5. Conclusion

New anomaly detection and localization method is presented, which uses position and neighborhood information for accurate estimation of the distribution of normal features. As a conditional probability, position information is modeled with accumulated histograms from features of normal training images. Likewise, the normal feature distribution given neighborhood information is modeled with MLP network. In addition, refinement algorithm using synthesized anomaly images is proposed to improve anomaly map according to the input image, which is the first refinement approach in anomaly detection and localization problem as far as the authors know. With various experiments, the overall performance and the effectiveness of the proposed approaches are shown.

References

- [1] Samet Akcay, Amir Atapour Abarghouei, and Toby P. Breckon. Ganomaly: Semi-supervised anomaly detection via adversarial training. *CoRR*, abs/1805.06725, 2018. 1
- [2] Paul Bergmann, Michael Fauser, David Sattlegger, and Carsten Steger. Mvtec ad — a comprehensive real-world dataset for unsupervised anomaly detection. In *2019 IEEE/CVF Conference on Computer Vision and Pattern Recognition (CVPR)*, pages 9584–9592, 2019. 1, 6
- [3] Niv Cohen and Yedid Hoshen. Sub-image anomaly detection with deep pyramid correspondences. *CoRR*, abs/2005.02357, 2020. 6
- [4] Diana Davletshina, Valentyn Melnychuk, Viet Tran, Hitansh Singla, Max Berrendorf, Evgeniy Faerman, Michael Fromm, and Matthias Schubert. Unsupervised anomaly detection for x-ray images, 2020. 1
- [5] Thomas Defard, Aleksandr Setkov, Angélique Loesch, and Romaric Audigier. Padim: a patch distribution modeling framework for anomaly detection and localization. *CoRR*, abs/2011.08785, 2020. 2, 6
- [6] Alexey Dosovitskiy, Lucas Beyer, Alexander Kolesnikov, Dirk Weissenborn, Xiaohua Zhai, Thomas Unterthiner, Mostafa Dehghani, Matthias Minderer, Georg Heigold, Sylvain Gelly, Jakob Uszkoreit, and Neil Houlsby. An image is worth 16x16 words: Transformers for image recognition at scale. *CoRR*, abs/2010.11929, 2020. 7
- [7] Denis Gudovskiy, Shun Ishizaka, and Kazuki Kozuka. Cflow-ad: Real-time unsupervised anomaly detection with localization via conditional normalizing flows. In *Proceedings of the IEEE/CVF Winter Conference on Applications of Computer Vision (WACV)*, pages 98–107, January 2022. 1, 6, 7
- [8] Chuan Guo, Geoff Pleiss, Yu Sun, and Kilian Q Weinberger. On calibration of modern neural networks. In *International conference on machine learning*, pages 1321–1330. PMLR, 2017. 4
- [9] Kaiming He, Xiangyu Zhang, Shaoqing Ren, and Jian Sun. Deep residual learning for image recognition. *CoRR*, abs/1512.03385, 2015. 2
- [10] Gao Huang, Zhuang Liu, Laurens Van Der Maaten, and Kilian Q Weinberger. Densely connected convolutional networks. In *Proceedings of the IEEE conference on computer vision and pattern recognition*, pages 4700–4708, 2017. 6, 7
- [11] Saif Imran, Yunfei Long, Xiaoming Liu, and Daniel Morris. Depth coefficients for depth completion. In *2019 IEEE/CVF Conference on Computer Vision and Pattern Recognition (CVPR)*, pages 12438–12447. IEEE, 2019. 6
- [12] Diederik P Kingma and Jimmy Ba. Adam: A method for stochastic optimization. In *ICLR*, 2015. 7
- [13] Jae-Han Lee and Chang-Su Kim. Multi-loss rebalancing algorithm for monocular depth estimation. In *European Conference on Computer Vision*, pages 785–801. Springer, 2020. 6
- [14] Chun-Liang Li, Kihyuk Sohn, Jinsung Yoon, and Tomas Pfister. Cutpaste: Self-supervised learning for anomaly detection and localization. *CoRR*, abs/2104.04015, 2021. 2
- [15] Pankaj Mishra, Riccardo Verk, Daniele Fornasier, Claudio Picciarelli, and Gian Luca Foresti. VT-ADL: A vision transformer network for image anomaly detection and localization. *CoRR*, abs/2104.10036, 2021. 6, 8
- [16] Duc Tam Nguyen, Zhongyu Lou, Michael Klar, and Thomas Brox. Anomaly detection with multiple-hypotheses predictions. In Kamalika Chaudhuri and Ruslan Salakhutdinov, editors, *Proceedings of the 36th International Conference on Machine Learning*, volume 97 of *Proceedings of Machine Learning Research*, pages 4800–4809. PMLR, 09–15 Jun 2019. 1
- [17] Stanislav Pidhorskyi, Ranya Almohsen, Donald A. Adjeroh, and Gianfranco Doretto. Generative probabilistic novelty detection with adversarial autoencoders. *CoRR*, abs/1807.02588, 2018. 1
- [18] Karsten Roth, Latha Pemula, Joaquin Zepeda, Bernhard Schölkopf, Thomas Brox, and Peter Gehler. Towards total recall in industrial anomaly detection. In *CVPR 2022*, 2022. 1, 2, 5, 6, 7
- [19] Marco Rudolph, Bastian Wandt, and Bodo Rosenhahn. Same same but different: Semi-supervised defect detection with normalizing flows. *CoRR*, abs/2008.12577, 2020. 1
- [20] Olga Russakovsky, Jia Deng, Hao Su, Jonathan Krause, Sanjeev Satheesh, Sean Ma, Zhiheng Huang, Andrej Karpathy, Aditya Khosla, Michael Bernstein, Alexander C. Berg, and Li Fei-Fei. ImageNet Large Scale Visual Recognition Challenge. *International Journal of Computer Vision (IJCV)*, 115(3):211–252, 2015. 2
- [21] Mohammad Sabokrou, Mohammad Khalooei, Mahmood Fathy, and Ehsan Adeli. Adversarially learned one-class classifier for novelty detection. *CoRR*, abs/1802.09088, 2018. 1
- [22] Mayu Sakurada and Takehisa Yairi. Anomaly detection using autoencoders with nonlinear dimensionality reduction. In *Proceedings of the MLSDA 2014 2nd Workshop on Machine Learning for Sensory Data Analysis, MLSDA’14*, page 4–11, New York, NY, USA, 2014. Association for Computing Machinery. 1
- [23] Ozan Sener and Silvio Savarese. Active learning for convolutional neural networks: A core-set approach. In *International Conference on Learning Representations*, 2018. 3
- [24] Samarth Sinha, Han Zhang, Anirudh Goyal, Yoshua Bengio, Hugo Larochelle, and Augustus Odena. Small-GAN: Speeding up GAN training using core-sets. In Hal Daumé III and Aarti Singh, editors, *Proceedings of the 37th International Conference on Machine Learning*, volume 119 of *Proceedings of Machine Learning Research*, pages 9005–9015. PMLR, 13–18 Jul 2020. 3
- [25] Hugo Touvron, Matthieu Cord, Alexandre Sablayrolles, Gabriel Synnaeve, and Hervé Jégou. Going deeper with image transformers. *CoRR*, abs/2103.17239, 2021. 7
- [26] Saining Xie, Ross B. Girshick, Piotr Dollár, Zhuowen Tu, and Kaiming He. Aggregated residual transformations for deep neural networks. *CoRR*, abs/1611.05431, 2016. 7
- [27] Jihun Yi and Sungroh Yoon. Patch SVDD: patch-level SVDD for anomaly detection and segmentation. *CoRR*, abs/2006.16067, 2020. 2, 6

- [28] Jiawei Yu, Ye Zheng, Xiang Wang, Wei Li, Yushuang Wu, Rui Zhao, and Liwei Wu. Fastflow: Unsupervised anomaly detection and localization via 2d normalizing flows. *CoRR*, abs/2111.07677, 2021. [1](#), [6](#), [7](#), [8](#)
- [29] Sergey Zagoruyko and Nikos Komodakis. Wide residual networks. *CoRR*, abs/1605.07146, 2016. [7](#)